ISSN 1392-3730/eISSN 1822-3605

VILNIUS TECH
Vilnius Gediminas Technical University

JOURNAL of CIVIL ENGINEERING and MANAGEMENT

2025
Volume 31
Issue 6
Pages 596–607
https://doi.org/10.3846/jcem.2025.24326

MODELLING PROGRESSIVE FAILURE OF SEGMENTAL LININGS IN SHIELD TUNNELS

Tianqi ZHANG, Bangguo HE, Zhitong CHEN✉, Xun LI, Gang ZHENG

MOE Key Laboratory of Coast Civil Structure Safety, Tianjin University, Tianjin 300072, China

Article History:
- received 19 February 2025
- accepted 31 March 2025

Abstract. Many engineering accidents in shield tunnels occur because localized failure induces the progressive damage or failure of segmental linings. At present, knowledge of the trigger mechanism for this catastrophe is still very limited. While it is difficult to conduct full-scale tunnel failure tests in actual strata, it is feasible to perform numerical simulations of tunnel failure. However, before simulating tunnel failure, it is important to establish a sophisticated model that considers the damage behaviour of segmental linings. In this paper, based on the concrete damage plasticity model and element deletion technology, a sophisticated model of segmental linings was established. The model was verified by data from current structural loading tests. To improve the calculation efficiency, the model was properly simplified. Then, it was applied to simulate the progressive failure of segmental linings due to localized failure in a shield tunnel considering complex soil-tunnel interactions. The numerical analysis showed that concrete was damaged in the segments adjacent to the localized failure zone. Some of the stirrups and erection bars in these segments yielded, while the upper and lower rows of steel bars as well as the bolts connecting the segments had sufficient safety redundancy.

Keywords: shield tunnel, CDP model, element deletion, damage of segmental lining, progressive failure, soil-tunnel interaction.

✉Corresponding author. E-mail: *chenzhitong1999@tju.edu.cn*

1. Introduction

With the rapid development of urban rail transit systems, shield tunnels undergo localized damage to varying degrees during construction and operation, and localized damage can induce progressive damage or failure (Zheng et al., 2015, 2017, 2024a). For example, the engineering accident of the Shanghai Metro Line 4 in 2003 started in a layer of water-rich sandy soil where the tunnel connecting passage was under construction, as shown in Figure 1a. Due to the failure of the refrigeration equipment and the freezing method applied, large amounts of water and sand leaked through the connecting passage into the upper and lower line tunnels, and there were severe losses of soil and water near the tunnel that prevented the tunnel from balancing the external loads acting on the structure, resulting in the collapse of a long portion of the tunnel. As shown in Figure 1b, the length of the progressive failure of the tunnel structure was approximately 274 m, and a series of related events, such as ground collapse and damage to surrounding buildings, resulted. Similarly, progressive failure accidents triggered by localized damage have been reported in Tianjin Metro Line 1 (Zhang et al., 2021) and Shanghai Metro Line 18 (Haorong et al., 2019), resulting in substantial economic losses. Therefore, understanding the failure mechanisms was crucial for engineering practice.

Restricted by cost, site conditions and other factors, the model tests adopted for investigating progressive tunnel damage or failure are usually reduced-scale tests. Some reduced-scale tests have been conducted to investigate the progressive failure characteristics and damage patterns of shield tunnel linings (Xu et al., 2024; Gong et al., 2024; Gao et al., 2024). Kiani et al. (2016) explored the damage of segmented tunnels under the action of normal faults through a series of centrifugal model tests. Cui (2017) investigated the effect of localized failure on adjacent tunnel segments in sandy soil layers by conducting tests with reduced-scale models. Weng et al. (2019) discussed the effect of loess stratum collapsibility on subway tunnel structures through centrifuge tests.

Reduced-scale tests work well for qualitative analysis, but full-scale experiments are required for quantitative analysis. There have been many studies on full-scale tests of shield tunnel linings (Liu et al., 2017, 2020; Qiu et al., 2021), and the internal force distribution, deformation, crack development and force transmission of individual segments have been deeply studied. However, most of the above tests considered only the structural and mechanical properties of the segment itself and did not con-

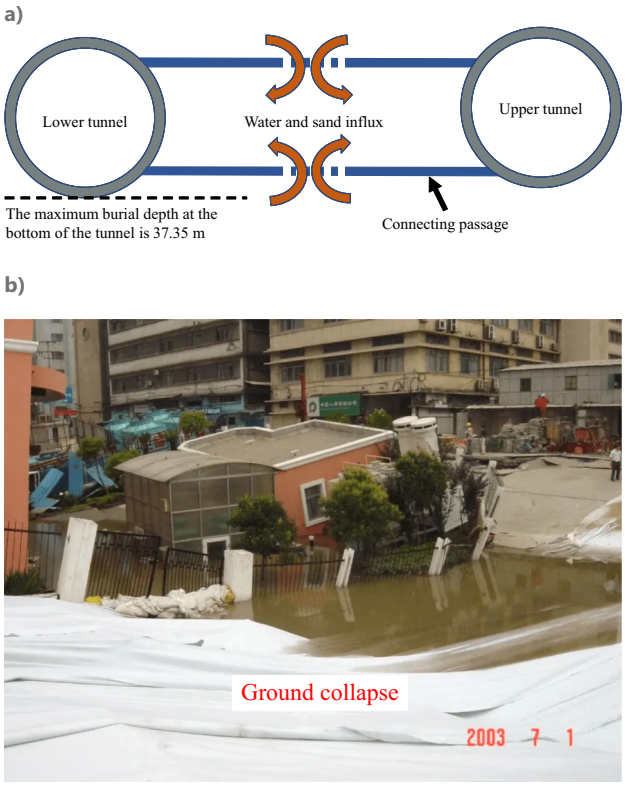

Figure 1. The Shanghai Metro Line 4 accident

sider the complex interaction between the soil stratum and tunnel structure. Thus, it is difficult to use these results to reflect actual progressive failure. Since it is very difficult to conduct full-scale tests in real strata, it is necessary to develop a sophisticated numerical model to simulate progressive failure in shield tunnels.

Many important achievements have been obtained in the study of shield tunnels by numerical simulation (Wang et al., 2014; Zhao et al., 2017; Yan et al., 2017, 2018; Ye & Liu, 2021; Zheng et al., 2024b), but there have been few numerical simulation studies on the progressive failure of full-scale tunnels that consider the complex interaction between the soil and structure. Cui (2017) used the discrete element method to simulate the loss of sand outside a shield tunnel. Zhu (2021) used the coupled Eulerian-Lagrangian (CEL) method to study the impact of the failure of one tunnel on an adjacent tunnel in sand and clay under different conditions. However, the above research adopted the shell-spring model to simulate the tunnel structure, and the segment damage mechanism and process were not revealed in detail. Therefore, it is necessary to establish a sophisticated tunnel model to explore the complex behaviour of the concrete, bolts and steel bars of the segments during progressive failure.

In this paper, a sophisticated segment model was established based on the concrete damage plasticity (CDP) model and element deletion technology. The segment was validated with data from current structural load tests. To improve the calculation efficiency, the segment model was properly simplified. Then, it was applied to simulate the damage of segmental linings due to localized failure in a shield tunnel considering complex soil-tunnel interactions. The results clarified the mechanism of progressive failure in the shield tunnel.

2. Establishment of a sophisticated segment model

2.1. Concrete damage plasticity (CDP) model

The CDP model embedded in ABAQUS software (Version 2020) is a continuous, plasticity-based model for isotropic damage to concrete. This model considers the main damage mechanism of concrete materials such as cracking damage due to tension and compression (Lubliner et al., 1989; Lee & Fenves, 1998). As a result, the evolution of the yield or damage surface of concrete is controlled by the compressive equivalent plastic strain $\tilde{\varepsilon}_c^{pl}$ and the tensile equivalent plastic strain $\tilde{\varepsilon}_t^{pl}$. Concrete materials undergo stiffness degradation due to damage, and the CDP model characterizes this degradation by employing the damage variables d_c and d_t (see Figure 2 and Figure 3).

The compressive behaviour of concrete in Figure 2 is divided into three main stages, with the dividing points being the initial compressive yield point σ_{c0} and the ultimate compressive stress σ_{cu}, after which the plastic strain continues to increase and the stiffness continues to degrade into the strain-softening stage. The tensile behav-

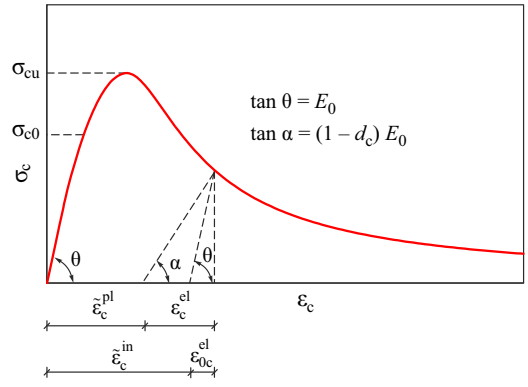

Figure 2. Uniaxial compressive stress–strain curve of concrete

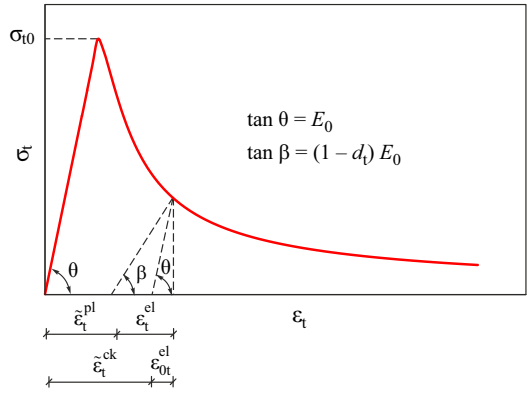

Figure 3. Uniaxial tensile stress–strain curve of concrete

iour of concrete in Figure 3 is divided into two stages, and the dividing point is the ultimate tensile stress σ_{t0}, after which the material directly enters the strain-softening stage. When the concrete material is unloaded from any point of the strain–softening phase of the stress-strain curve, stiffness degradation occurs. The relationships between the equivalent plastic strains $\tilde{\varepsilon}_c^{pl}$ and $\tilde{\varepsilon}_t^{pl}$ and the inelastic strains $\tilde{\varepsilon}_c^{in}$ and cracking strains $\tilde{\varepsilon}_t^{ck}$ are as follows:

$$\tilde{\varepsilon}_c^{pl} = \tilde{\varepsilon}_c^{in} = \frac{d_c}{(1-d_c)}\frac{\sigma_c}{E_0}; \tag{1}$$

$$\tilde{\varepsilon}_t^{pl} = \tilde{\varepsilon}_t^{ck} = \frac{d_t}{(1-d_t)}\frac{\sigma_t}{E_0}. \tag{2}$$

2.2. Determination of CDP model parameters

The elastic phase of the CDP model for concrete is controlled by the elastic modulus E_0. The stress–strain relationship in the inelastic phase is referred to in the Code for Design of Concrete Structure in China (Ministry of Housing and Urban-Rural Development of the People's Republic of China, 2002).

When concrete undergoes compression, $\beta_c = \tilde{\varepsilon}_c^{pl} / \tilde{\varepsilon}_c^{in}$; combined with Figure 2 and Eqn (1), this yields the CDP model compressive damage factor:

$$d_c = \frac{(1-\beta_c)\tilde{\varepsilon}_c^{in} E_0}{\sigma_c + (1-\beta_c)\tilde{\varepsilon}_c^{in} E_0}. \tag{3}$$

Similarly, letting $\beta_t = \tilde{\varepsilon}_t^{pl} / \tilde{\varepsilon}_t^{ck}$ yields the tensile damage factor of the CDP model:

$$d_t = \frac{(1-\beta_t)\tilde{\varepsilon}_t^{ck} E_0}{\sigma_t + (1-\beta_t)\tilde{\varepsilon}_t^{ck} E_0}. \tag{4}$$

Taking the stress σ_{c0} at the compressive elastic–plastic partition point of concrete as 0.4 σ_{cu} (Lu et al., 2015), the modulus of elasticity E_0 of C50 concrete is calculated as 34.18 GPa. Additionally, taking the parameters β_c as 0.7 and β_t as 0.95 (Zhang et al., 2008), the parameters of the CDP model are calculated and shown in Table 1.

The detailed plastic parameters of concrete were presented in Table 2.

2.3. Concrete element failure deletion

ABAQUS has a general framework for material failure modelling (Dassault Systémes Simulia Corp., 2020) that allows a combination of multiple failure mechanisms to act simultaneously on a material cell. The user subroutine VUSDFLD supports the redefinition of field variables at material points, which allows the simulation to retrieve the number of material points at the beginning of the material increment without affecting the material properties and to make decisions about material failure and whether to delete an element. Rodríguez Soler et al. (2013) chose equivalent plastic strain as the variable for the criterion to decide whether concrete elements had undergone failure and successfully implemented this method to delete failed concrete elements: the concrete element failure deletion (CEFD) method. Wang (2017) removed a concrete element from a simulation when its damage variable value reached 0.99. From the foregoing examples, it can be seen that the equivalent plastic strain and the concrete damage variables are in one-to-one correspondence and are interchangeable.

In this paper, the VUSDFLD subroutine was written to control the deletion of concrete elements by using two parameters, the equivalent compressive plastic strain $\tilde{\varepsilon}_c^{pl}$ and equivalent tensile plastic strain $\tilde{\varepsilon}_t^{pl}$. For C50 grade concrete, the deletion criterion for concrete cells was set as follows: elements were deleted when $\tilde{\varepsilon}_c^{pl} > 0.014$ or $\tilde{\varepsilon}_t^{pl} > 0.007$.

Table 1. Calculated parameters of the CDP model for concrete materials

Compressive strength/MPa	Inelastic strain/10^{-3}	d_c	Tensile strength/MPa	Cracking strain/10^{-3}	d_t
12.96	0.000	0.000	2.64	0.000	0.000
20.71	0.065	0.031	1.68	0.106	0.070
27.20	0.210	0.073	1.12	0.195	0.172
31.10	0.431	0.124	0.85	0.272	0.278
32.40	0.728	0.187	0.67	0.356	0.391
27.65	1.537	0.363	0.56	0.438	0.486
18.50	2.809	0.608	0.46	0.540	0.583
11.28	4.526	0.804	0.22	1.373	0.883
6.19	7.511	0.925	0.11	3.678	0.977
1.37	28.103	0.995	0.06	7.654	0.993

Table 2. Plastic parameters of the concrete

Parameters	Dilation angle Ψ	K_c	Viscosity μ	f_{b0}/f_{c0}	Flow potential eccentricity ε
Value	38 (°)	0.667	0.0005	1.16	0.1

3. Validation of the sophisticated model

3.1. Selected benchmark tests

A sophisticated segment model based on the CDP model and the CEFD method has been described in detail in the previous section, but the accuracy and reliability of its application in actual tunnel lining structure analysis must be verified. Therefore, following the example of Zhou (2011), one-segment and two-segment tests were selected to verify the correctness of the abovementioned concrete parameters and CEFD criterion and the three-segment test of Liu et al. (2018) was used to validate the applicability of the sophisticated segment model in simulations of the damage behaviour of segments between adjacent rings in a shield tunnel.

The one-segment test (Mašín, 2005) obtains various mechanical properties of a full-scale standard reinforced concrete specimens. The outer diameter of the segment is 6000 mm, the thickness is 300 mm, the width is 1200 mm, and the annular centre angle of the lining segment is 67.5°. As shown in Figure 4a, this study mainly considered two groups of experiments, Pzw1 and Pzw2, with different constraints. In terms of loading, three parallel jacks were used to exert equal radial point forces on the segment, the action point was at the quarter point of the arc surface, and the load level was controlled by the mid-span deflection of the segment. The corresponding segment concrete label was C50; see Zhou (2011) for more details.

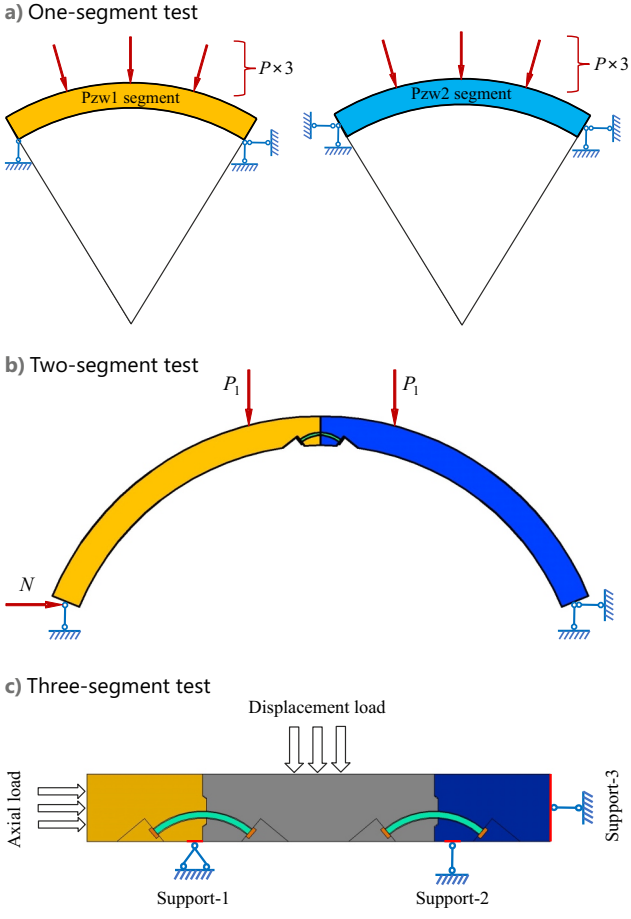

Figure 4. Loading force diagram of the selected benchmark tests

For the two-segment mechanical test (Zhou, 2011), the segments have the same material and segment structure as those used in the one-segment test. The two segments are connected by two curved bolts to form a symmetrical structure. The material of the bolts is M24. The centre angle of the ring is 76°, and the preload is 20 kN. The loading mode and constraints of the test are shown in Figure 4b. The test stipulates that the bending moment of the intrados of the segment at the joint is positive, and the corresponding eccentricity is positive. In this study, the positive bending moment test with an eccentricity of +0.15 m was used. For more details, see Zhou (2011).

In the three-segment test (Liu et al., 2018), the outer diameter of the segment is 6200 mm, the thickness is 350 mm, the width is 1200 mm, and the central angle of the lining segment is 18.5°. The bolts are M30 round bolts of grade 5.8. The axial force between the longitudinal segments of the tunnel is simulated by force loading. An axial force of 130 kN is applied in the test, and then the shear effect between rings is simulated by displacement loading. The boundary conditions of the model are controlled by the three supports shown in Figure 4c to constrain the displacement of the corresponding concrete surface. See Liu et al. (2018) for more details.

3.2. Comparison between numerical results and test data

3.2.1. One-segment test

To accurately simulate the structure of the segment, the concrete and steel were modelled by the C3D8R solid element and the T3D2 truss element, respectively, and the ABAQUS dynamic explicit algorithm was used to reflect the real force characteristics of the segment. The steel cage was embedded in the concrete to simulate the interaction between the steel and concrete. For C50 concrete, the elastic modulus was taken as 34.18 GPa, and Poisson's ratio was 0.2.

The segment load-deflection curve is shown in Figure 5. The numerical simulation deflection values of the two groups of segments at the three characteristic points of the test cracking load, yield load and ultimate load were in good agreement with the experimental values.

For Pzw1, the deflection in the span initially increased linearly with the load, but after reaching the cracking load, the deflection increased nonlinearly with the load. The deflection increased faster until failure was detected in the liner of the concrete elements in the intrados, and equidistant symmetric cracks appeared. As the loading reached the ultimate load of 185 kN, the cracks in the lining continued to expand, and the deflection continued to increase until the lining was completely destroyed, which was consistent with the deformation damage process of the test. For Pzw2, since the lining was subjected to axial force, its bearing capacity was greatly improved compared with that of Pzw1, and the ultimate load reached 1050 kN. The load-

deflection curves of the Pzw2 simulation and test were basically the same, and the relative error between them was within 5%, which was in good agreement.

In addition to the deformation of the segment structure, Figure 6 shows the variation in the steel bar strain with load for the two groups of segments, and Figure 7 shows the variation in the mid-span concrete strain with load. The error of the simulation results was within the acceptable range.

3.2.2. Two-segment test

The two-segment mechanical model used the same material for the segments and segment structure simulation method as the one-segment mechanical model. To simulate the structure of the joint with as much detail as possible, the joint form shown in Figure 8 was adopted. The bolts were M24 round bolts that initially had no contact with the bolt holes. The interaction between the components at the joint was simulated by "hard" contact in the normal direction and a tangential penalty function with a friction coefficient of 0.4. The C3D8R solid element was used to model the bolts; the corresponding elastic modulus was 200 GPa, Poisson's ratio was 0.167, and the pretightening force was 20 kN.

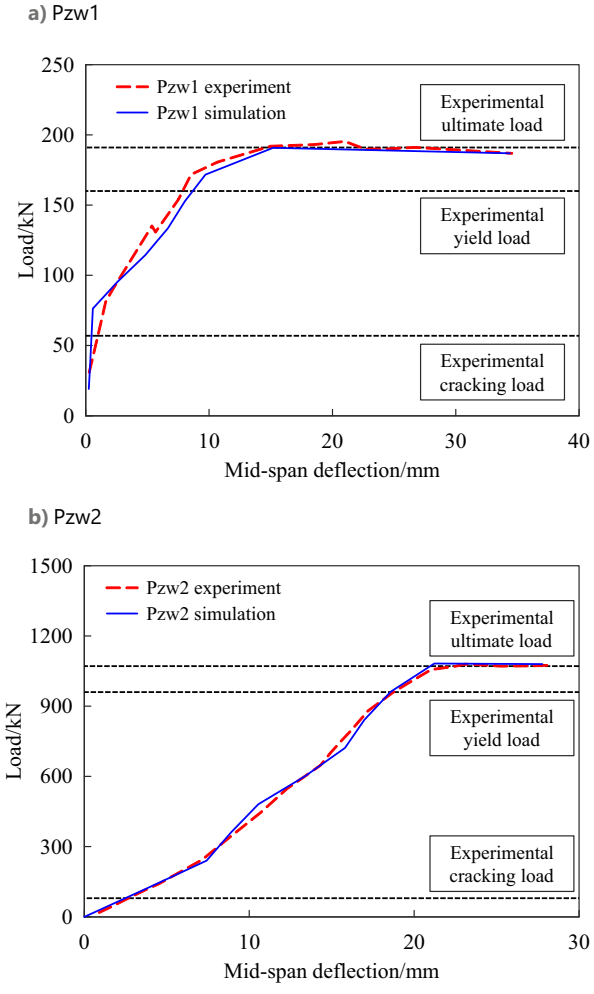

Figure 5. Load-deflection curves from the one-segment test

To verify the applicability of the CEFD method in the mechanical model of the two-segment test, the main focus was on the performance of the model joint. As the load increased, the vertical displacement at the segment joint also increased gradually, the extrados of the joint squeezed each other, and the joint bending moment was mainly borne by the bolts. During the loading period, concrete element failure and deletion occurred at the edge of the concrete in the compression zone, corresponding to local crushing and spalling of the test concrete. The segments in the tension zone formed an open angle; the specific values are shown in Figure 9.

To evaluate the simulation of the model, the bending stiffness of the joint was considered. Referring to the method of Zhou (2011), the relationship between the joint opening angle θ and the joint bending moment M was divided into a curved section and a linear section, and the bending stiffness k_θ of the joint was calculated according to Eqn (5) and Eqn (6).

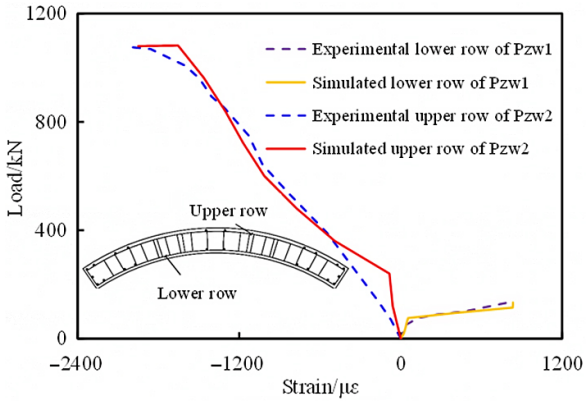

Figure 6. Load-strain curves of the steel bars

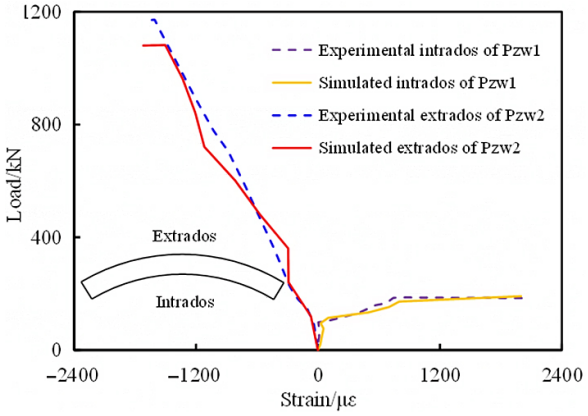

Figure 7. Load-strain curves of the concrete at the mid-span

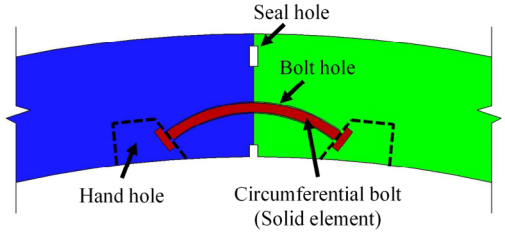

Figure 8. Joint form of the two-segment test

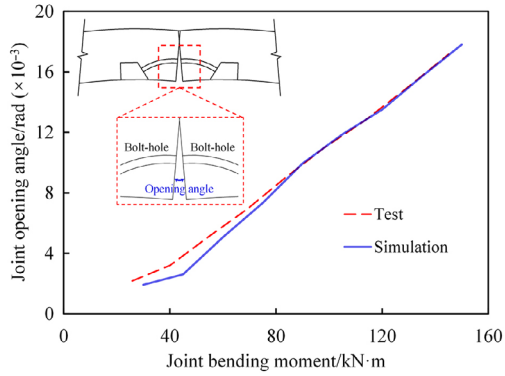

Figure 9. The relationship between the joint opening angle and the bending moment of the two-segment test

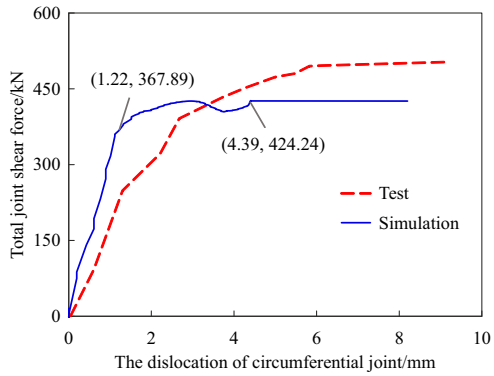

Figure 10. The relationship between the total joint shear force and the dislocation of the circumferential joint of the three-segment test

$$M = \begin{cases} k_0\theta + k_1 & N \geq 600\ \text{kN} \\ k_2\theta^2 + k_3\theta + k_4 & N < 600\ \text{kN} \end{cases}; \quad (5)$$

$$k_\theta = \frac{dM}{d\theta}\begin{cases} k_0 & N \geq 600\ \text{kN} \\ \sqrt{k_3^2 + 4k_2\left(M - k_4\right)} & N < 600\ \text{kN} \end{cases}, \quad (6)$$

where k_0, k_1, k_2, k_3 and k_4 are the fitting coefficients.

The flexural stiffness of the straight line obtained from the model calculation result was 7539 kN·m·rad^{-1}, which was 0.54% different from the test result, indicating that the calculation result was close to the test result in the straight section. The bending stiffness of the model curve section ranged from 6667 to 11811 kN·m·rad^{-1}. Table 3 shows that the error between the model and test results was relatively large, but it was within an acceptable range. The reason for the large error may be that the model was simplified; for example, the influence of the rubber pad was not considered.

Table 3. Calculation result of the flexural stiffness of the joint in the curved section of the mechanical model of the two-segment test

Flexural stiffness/kN·m·rad^{-1}	Test	Simulation	Error
Minimum	6771	6667	−15.36%
Maximum	9976	11811	18.39%

3.2.3. Three-segment test

The relationship between the total shear force of the left and right joints and the dislocation are shown in Figure 10. According to the deformation characteristics of the model, the shear failure of the joints can be roughly divided into two stages. In the first stage, affected by the horizontal axial force, the shear force of the joints is mainly provided by the friction force between the concrete surfaces, and the shear force of the segment is transmitted to the bolts through the bolt head so that the bolts bear a small amount of shear force. In the second stage, the displacement of the joint reaches 1.22 mm. After the groove and tongue come in contact, the shear force of the joint further increases, and the joint stiffness is relatively large in this stage. Afterwards, the joint groove and tongue of the left and right circumferential are damaged to varying degrees, and the shear stiffness decreases. Overall, the shear force borne by the bolts is limited, and the shear force is mainly provided by friction between the concrete surfaces and the contact force between the groove and tongue. The shear stiffness of the joints in the first stage of the simulation results was slightly larger than that of the test, while the ultimate shear bearing capacity was 15.7% smaller than that of the test, which may have been caused by test loading and measurement errors.

4. Simplified segment model and its validation

4.1. Simplification

Due to limited computing power, it is impossible to use the overly sophisticated model in the calculations of shield tunnels. Thus, it is necessary to reasonably simplify the model, especially the bolt parts. In this study, a new equivalent form of bolts was proposed, as shown in Figure 11, which simplified the joint by mainly considering the following aspects:

(1) The round bolts (round bolt holes) were changed to square bolts (square bolt holes) with a square cross section, and the side length was equal to the diameter of the round bolts (round bolt holes).

(2) One curved bolt was changed to two semi-straight bolts, and the semi-straight bolts were connected through 4 sets of connector elements.

(3) The shape of the hand hole was adjusted to achieve an optimized meshing scheme.

As shown in Figure 11c, the tensile and shear behaviours of the connector elements participated in the corresponding behaviour of the joints. The tensile stiffness of each set of connector elements in the simplified model was 3747 kN/m (this value was determined based on the principle of stiffness equivalence). The shear stiffness k_s was obtained by using Eqn (7), and the shear stiffness of each set of connector elements was $k_s/4$:

$$k_s = \frac{EA}{2\left(1+\mu\right)\delta}, \quad (7)$$

where E, A, and μ are the elastic modulus, cross-sectional area, and Poisson's ratio of the bolt, respectively, and δ is the tensile displacement, as shown in Figure 12.

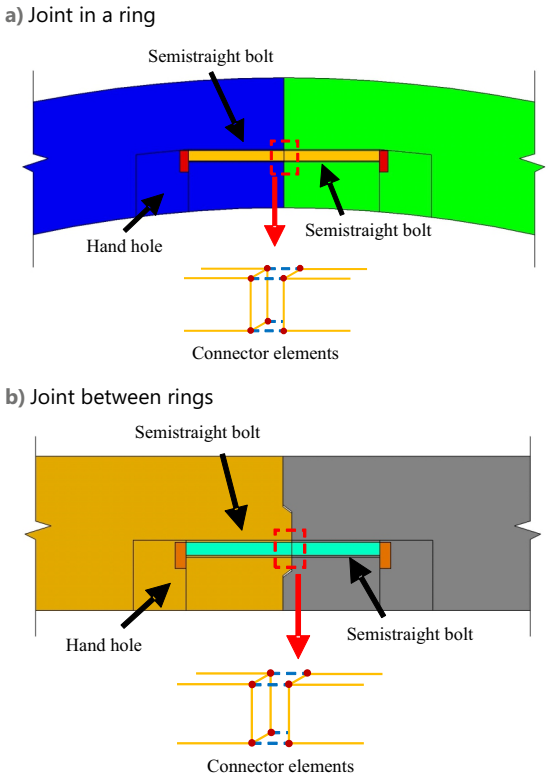

Figure 11. Equivalent model of bolts

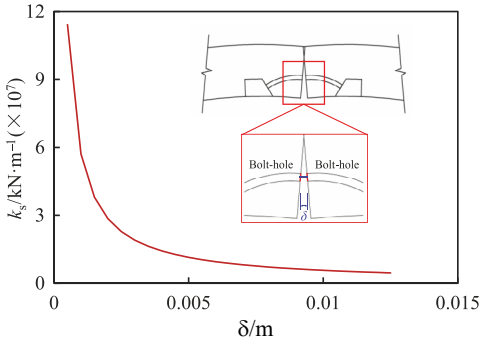

Figure 12. Relationship between shear stiffness and δ

4.2. Validation

Two additional sets of simulations (TS-2 and TS-3) were carried out referring to the previously mentioned two-segment and three-segment tests to validate the reliability of the simplified model. Different from the two-segment test performed by Zhou (2011) and the three-segment test performed by Liu et al. (2018), the tunnel segment size was 6200 mm in outer diameter and 350 mm in thickness (a typical segment size). In TS-2, the segment ring angle was 67.5° and the joint eccentricity was +0.17 m. In TS-3, the centre angle of the segment between rings was 22.5° and the axial force was proportionally changed to 158 kN.

To simulate the pretightening force applied to the bolts in the actual project, referring to Zhou (2011), a uniform pretightening force of 20 kN was applied to the bolts. For the steel bars, the upper and lower rows of steel bars were HRB400 grade with a diameter of 25 mm, and the other steel bars were HPB300 grade with a diameter of 10 mm. The bolts were M30 bolts of grade 8.8, the elastic modulus was 210 GPa, and Poisson's ratio was 0.3.

The results obtained with the simplified model and the sophisticated model are compared in Figure 13. In the simulation of TS-2 and TS-3, the maximum discrepancy was approximately 25% and 9%, respectively, which were deemed to be acceptable. However, the simplified model provided a significant improvement in the calculation speed, which greatly shortened the calculation time. As shown in Table 4 and Table 5, the calculation of the sophisticated models and the simplified models were both performed on the same workstation with 64.0 GB of memory and 2 Intel Xeon processors (16 cores) at 3.40 GHz. The computation time of the simplified models was greatly reduced compared to that of the sophisticated models. In the simulation of TS-2, the calculation time of the simplified model was reduced by 74.5% compared with that of the corresponding sophisticated model, and the calculation time in the simulation of TS-3 was reduced by 66.3%.

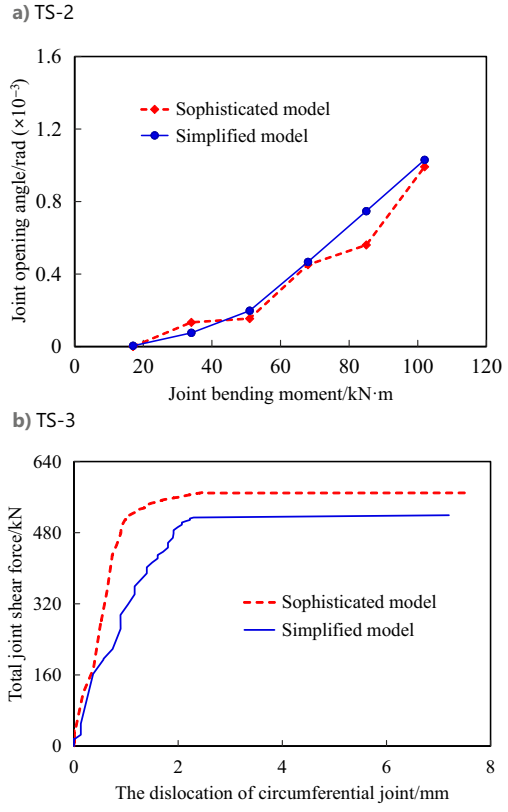

Figure 13. Comparison of results obtained by the simplified models and sophisticated models

Table 4. Comparison of the TS-2 sophisticated model and simplified model

Project		Sophisticated model	Simplified model	Simplified model compared to sophisticated
Total number of nodes		68610	35980	Decrease by 47.6%
Number of elements	Solid element	51942	25032	Decrease by 51.8%
	Connector element	10428	6200	Decrease by 40.5%
Minimum element size/m		0.00495	0.03	Increase by 506.1%
Minimum stable time increment		6.96E–07	3.06E–06	Increase by 339.7%
Average actual time spent in step calculation per second/s		4238	1079	Decrease by 74.5%

Table 5. Comparison of the TS-3 sophisticated model and simplified model

Project		Sophisticated model	Simplified model	Simplified model compared to sophisticated
Total number of nodes		28427	12842	Decrease by 54.8%
Number of elements	Solid element	19280	8340	Decrease by 56.7%
	Connector element	5504	2166	Decrease by 60.6%
Minimum element size/m		0.0115	0.02	Increase by 73.9%
Minimum stable time increment		1.30E–06	3.30E–06	Increase by 153.8%
Average actual time spent in step calculation per second/s		2010	678	Decrease by 66.3%

5. Simulating failure of segmental linings due to localized failure in shield tunnels

5.1. Numerical model

Based on the simplified model, a semisymmetrical tunnel model was established, as shown in Figure 14. The model tunnel was composed of 10.5 rings in total, HR and R1 to R10, as shown in Figure 14b. The segment was assembled with staggered joints, and the joint form and parameters were consistent with those given in Section 4.1. To consider the interaction between the soil and structure, referring to Zhu (2021), the model adopted the CEL method to simulate the soil and tunnel. That is, the tunnel was modelled by Lagrangian elements, and the soil was simulated by Eulerian body flowing in a fixed grid. For the model boundary, used to prevent soil loss, velocity constraints were imposed at the bottom and around the model, and a void space was set at the top of the model. The thickness of the overlying soil layer on the tunnel was 2*D*, and *D* was the outer diameter of the tunnel. The interaction between the components was simulated by "hard" contact in the normal direction, the tangential penalty function corresponded to the friction coefficient, which was taken as 0.4, and the bolt was preloaded with 20 kN. A constitutive model of the soil that combined generalized hypoplastic theory with critical state soil mechanics was adopted (Mašín, 2005). The specific parameters are shown in Table 6 (Zhu, 2021). The calculation of the model was divided into two parts. In the first part, the model was under the action of 1 g gravity to balance the soil pressure. In the second part, the red segment in Figure 14b was set as the site of initial failure to simulate localized failure of the tunnel. Then, the response of the entire structure was obtained accordingly.

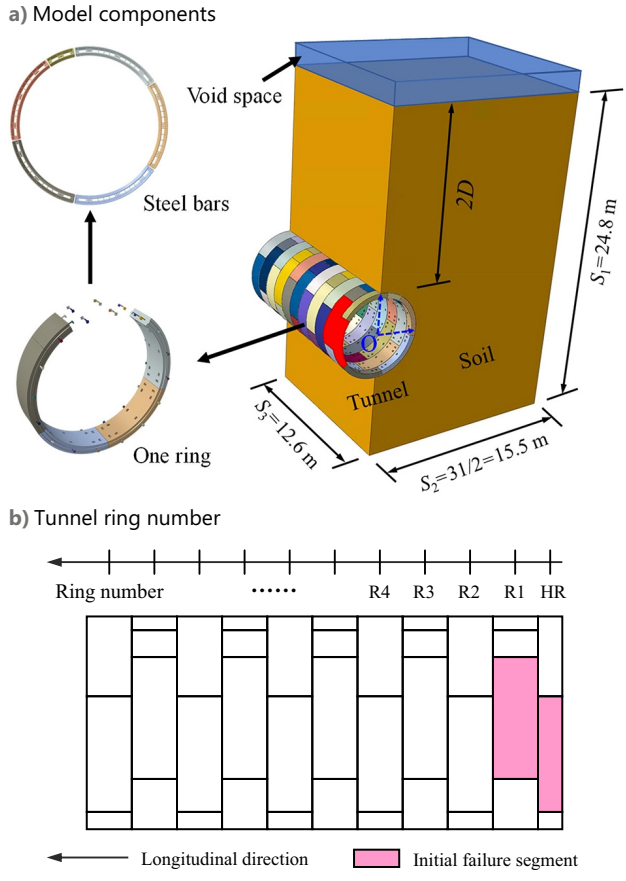

Figure 14. Numerical model

Table 6. Soil parameters

γ (g/cm^3)	*N*	λ*	φ_c (°)	κ*	υ
1.621	0.918	0.065	27.5	0.01	0.35

5.2. Results and analysis

5.2.1. Distribution of structural damage in the shield tunnel

When initial failure occurred in a shield tunnel, the soil stress around the tunnel changed first. Figure 15a shows the soil pressure after localized failure of the tunnel when a soil unloading area formed around the tunnel due to soil loss. The minimum soil pressure in the unloading area was close to zero, indicating that the soil had undergone a large disturbance. Figure 15b shows that the direction of the principal stress of the soil around the tunnel was deflected, indicating that a soil arch was formed.

As localized failure occurred, the state of the tunnel concrete element also changed. As shown in Figure 16, the damage to the tunnel concrete occurred not only in the HR and R1 rings where the initial failure segments were located but also the R2 ring, and the damage was mainly concentrated in the first few rings. A small part of the concrete was damaged in the R3 tunnel ring, and basically none of the concrete elements after the R4 ring were damaged. A comparison of the compressive and tensile concrete damage diagrams in Figure 16 shows that the compressive and tensile damaged areas of the concrete were basically the same, i.e., the failure of the tunnel was the result of the combined action of compressive and tensile damage.

a) Soil pressure

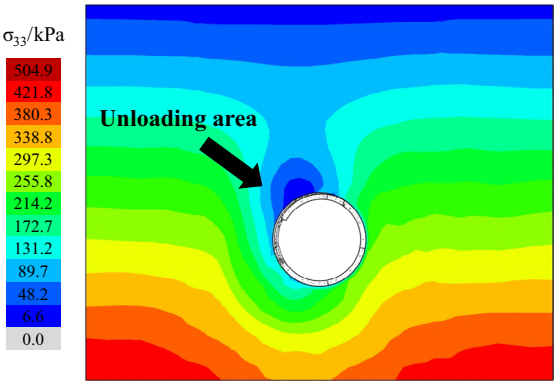

b) Computed principal stress orientations

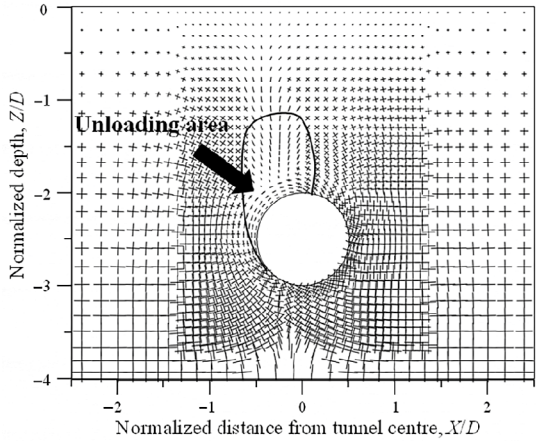

Figure 15. Response of strata after localized failure

a) Damage due to concrete compression

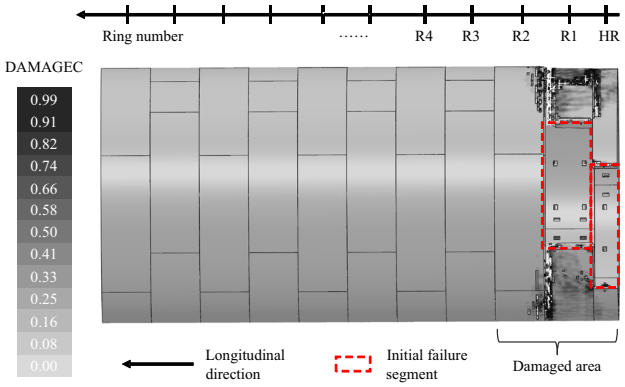

b) Damage due to concrete tension

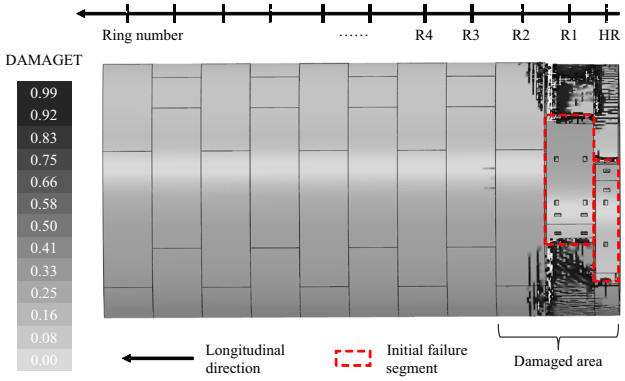

Figure 16. Damage in the tunnel segment

5.2.2. Analysis of the evolution of the structural behaviour of the damaged linings

The previous analysis shows that the main structural damage of the tunnel was concentrated among a few adjacent rings, namely, the HR, R1, and R2 rings. In this section, these damaged tunnel rings are analysed in detail.

Figure 17 shows a schematic diagram of the damaged area of the concrete in the destroyed ring lining segment. The damage was mainly distributed in the segment area that was closer to the segment where initial failure occurred. The concrete at the farthest distance from the initial failure segment ring was not damaged.

Accompanying the concrete damage was the deformation of the reinforcing bars inside the segment. Figure 18 shows the stress contour plot of the reinforcing bars in the segments. In general, the upper and lower rows of steel bars were not close to their yield strength, and only some of the stirrups and erection bars yielded in the area where concrete was damaged. Therefore, the design for the upper and lower rows of steel bars is sufficient for engineering applications, while the stirrups and erecting bars for the weak part of the segment ring should be properly enhanced.

The von Mises stress nephograms of the bolts in and between the failed rings are given in Figure 19a. The figure shows that the maximum stress of the tunnel bolts was 119.5 MPa, and their yield strength was 640 MPa, indicat-

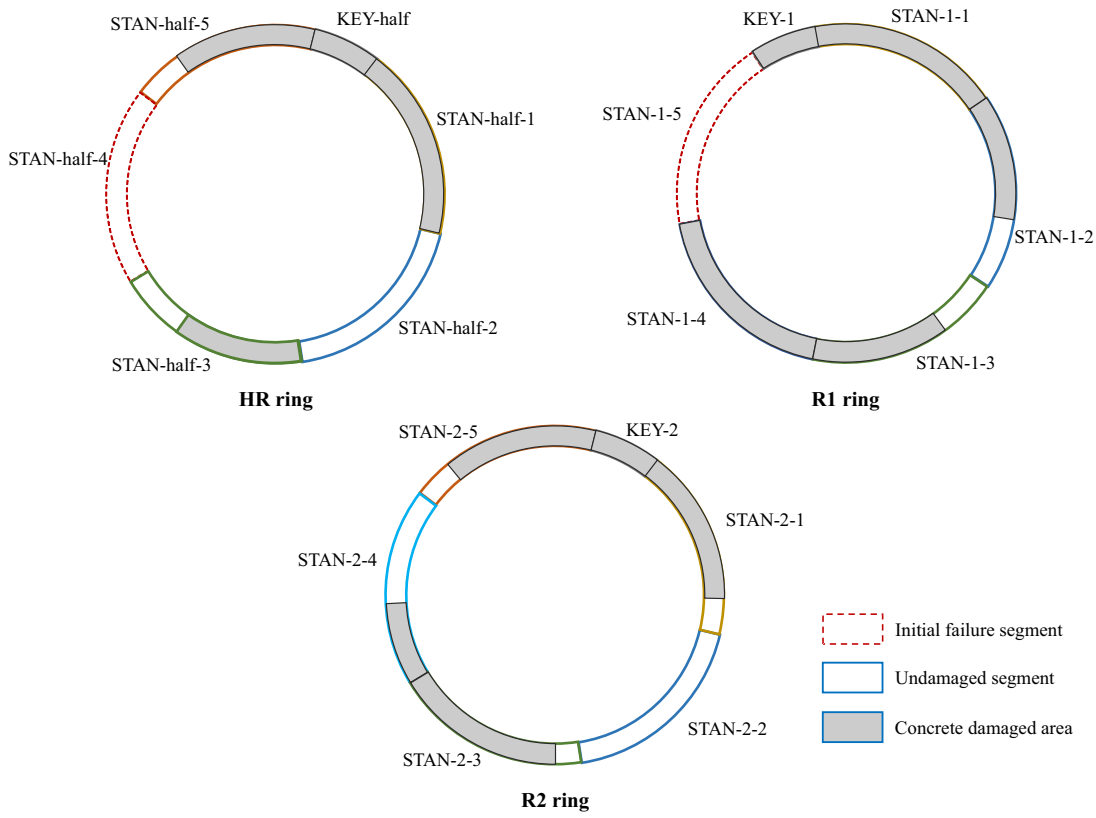

Figure 17. The damage distributions in segment rings

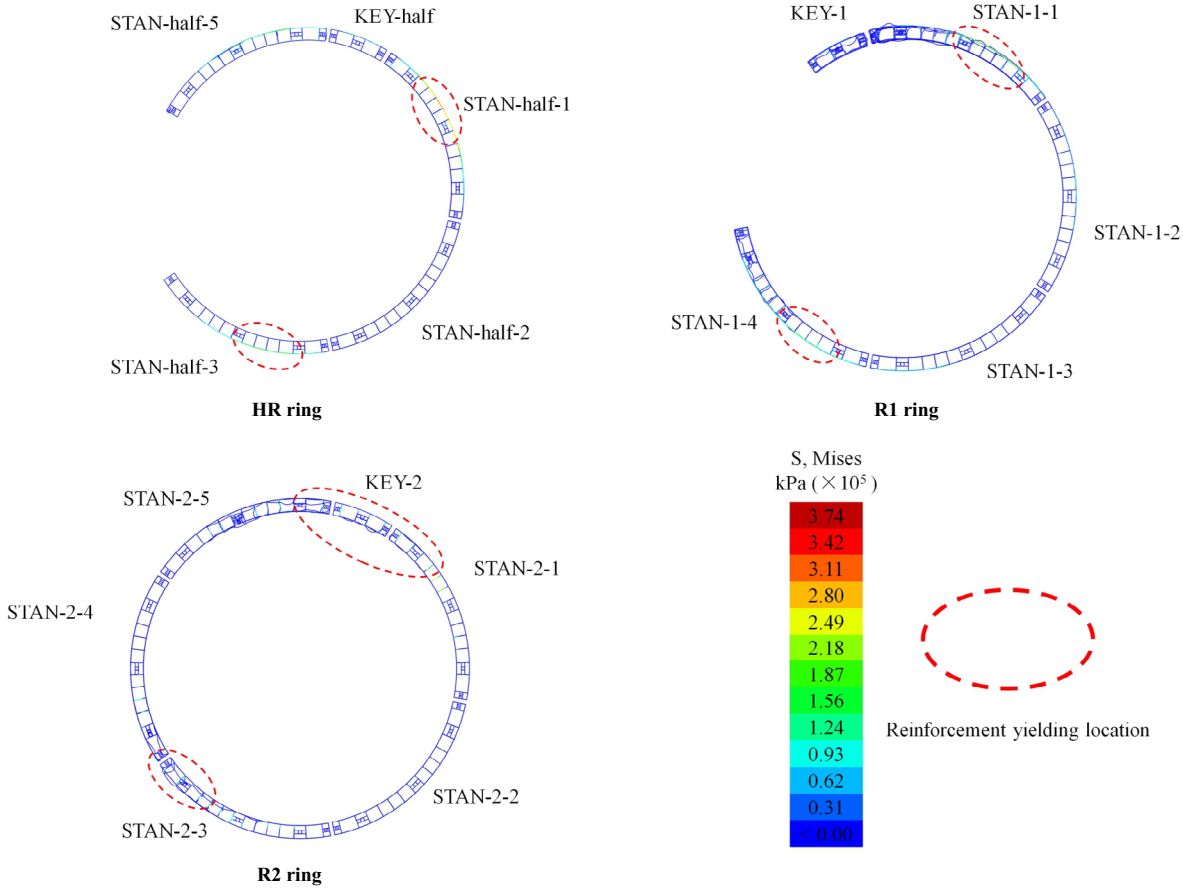

Figure 18. The stress on steel bars in segment rings

ing that even when the concrete was damaged, the bolts had not been damaged or even yielded. This was consistent with observations in engineering applications (Figure 19b shows a ruined segment at the site of a tunnel accident in Tianjin, and it is clear that the bolts did not break after the concrete was damaged). This further showed that the design strength of the bolts was sufficient.

a) Von Mises stress of the bolts

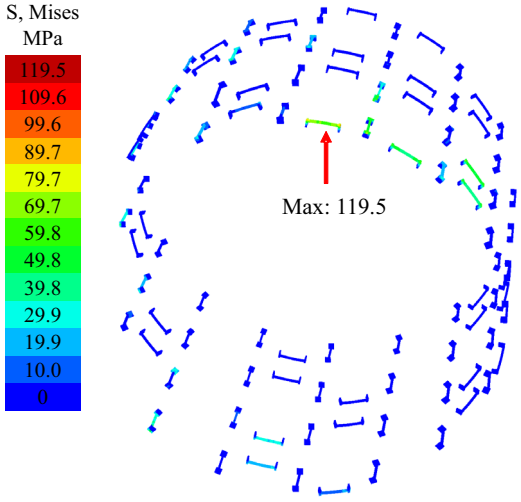

b) Damaged concrete and unbroken bolt observed in an accident

Figure 19. Bolt states under tunnel failure obtained by numerical simulation and observed in practical engineering

6. Conclusions

To facilitate research on the progressive failure of segmental linings in shield tunnels due to localized failure, a series of simulation approaches were employed and developed in this paper. Basically, the following conclusions can be drawn:

(a) To realistically simulate the crushing and spalling behaviours of concrete, element deletion technology was incorporated in combination with the CDP model in the analysis. A sophisticated finite element model was established and compared with test data. The results showed that the sophisticated model was feasible for simulating the mechanical behaviours of segment linings, which included one-segment, two-segment and three-segment tests.

(b) The sophisticated model was properly simplified mainly through the equivalence of the bolts. It was shown that, compared with the sophisticated model, the simplified model can reduce the calculation time by 66%, and that the error in the results was within the acceptable range.

(c) The simplified model was used to simulate the progressive failure of segmental linings in shield tunnels due to localized failure, which involved a large number of nodes and elements and the complex soil-tunnel interaction. The numerical results showed that the stirrups and erection bars at the weak part of the segment ring should be enhanced, while the upper and lower rows of steel bars and bolts have sufficient redundancy of safety and do not require additional reinforcement.

Data availability statement

Some or all data used in this study are available from the corresponding author upon reasonable request.

Funding

The authors would like to acknowledge financial support from the National Natural Science Foundation of China (Grant No. 52478408), the Creative Research Groups of National Natural Science Foundation of China (No. 52421005), the Tianjin Research Innovation Project for Postgraduate Students (Grant No. 2021YJSS035).

Disclosure statement

No potential conflict of interest was reported by the authors.

References

Cui, T. (2017). *Study on the mechanism and prevention of progressive failure of shield tunnel induced by local failure* [Doctoral thesis]. Tianjin University, Tianjin.

Dassault Systémes Simulia Corp. (2020). *SIMULIA user assistance* (Version 2020).

Gao, X., Li, P., Zhang, M., Wang, H., Jia, Z., & Feng, W. (2024). Effect of local openings on bearing behavior and failure mechanism of shield tunnel segments. *Underground Space*, *16*, 183–205. https://doi.org/10.1016/j.undsp.2023.10.006

Gong, C., Xie, C., Zhu, H., Ding, W., Song, J., & Ge, Y. (2024). Time-varying compressive properties and constitutive model of EPDM rubber materials for tunnel gasketed joint. *Construction and Building Materials*, *433*, Article 136734. https://doi.org/10.1016/j.conbuildmat.2024.136734

Haorong, C., Limin, P., Mingfeng, L., Fudong, C., & Qianlong, T. (2019). Causes analysis, reinforcement and repair technology of segment crack and damage during shield tunnelling process: A case study. *Geotechnical and Geological Engineering*, *37*, 765–773. https://doi.org/10.1007/s10706-018-0648-y

Kiani, M., Akhlaghi, T., & Ghalandarzadeh, A. (2016). Experimental modeling of segmental shallow tunnels in alluvial affected by normal faults. *Tunnelling and Underground Space Technology*, *51*, 108–119. https://doi.org/10.1016/j.tust.2015.10.005

Lee, J., & Fenves, G. L. (1998). Plastic-damage model for cyclic loading of concrete structures. *Journal of Engineering Mechanics*, *124*(8), 892–900. https://doi.org/10.1061/(ASCE)0733-9399(1998)124:8(892)

Liu, X., Dong, Z., Bai, Y., & Zhu, Y. (2017). Investigation of the structural effect induced by stagger joints in segmental tunnel linings: First results from full-scale ring tests. *Tunnelling and Underground Space Technology*, *66*, 1–18. https://doi.org/10.1016/j.tust.2017.03.008

Liu, X., Dong, Z., Song, W., & Bai, Y. (2018). Investigation of the structural effect induced by stagger joints in segmental tunnel linings: Direct insight from mechanical behaviors of longitudinal and circumferential joints. *Tunnelling and Underground Space Technology*, *71*, 271–291. https://doi.org/10.1016/j.tust.2017.08.030

Liu, X., Zhang, Y., & Bao, Y. (2020). Full-scale experimental investigation on stagger effect of segmental tunnel linings. *Tunnelling and Underground Space Technology*, *102*, Article 103423. https://doi.org/10.1016/j.tust.2020.103423

Lubliner, J., Oliver, J., Oller, S., & Onate, E. (1989). A plastic-damage model for concrete. *International Journal of Solids and Structures*, *25*(3), 299–326. https://doi.org/10.1016/0020-7683(89)90050-4

Lu, X. Z., Ye, L. P., & Miao, Z. W. (2015). *Elasto-plastic analysis of buildings against earthquake*. China Architecture and Building Press.

Mašín, D. (2005). A hypoplastic constitutive model for clays. *International Journal for Numerical and Analytical Methods in Geomechanics*, *29*(4), 311–336. https://doi.org/10.1002/nag.416

Ministry of Housing and Urban-Rural Development of the People's Republic of China. (2002). *Code for design of concrete structures* (GB 50010-2002).

Qiu, Y., Hu, X., Walton, G., He, C., He, C., & Ju, J. W. (2021). Full scale tests and a progressive failure model to simulate full mechanical behavior of concrete tunnel segmental lining joints. *Tunnelling and Underground Space Technology*, *110*, Article 103834. https://doi.org/10.1016/j.tust.2021.103834

Rodríguez Soler, J., Martinez Cutillas, F. J., & Marti Rodriguez, J. (2013). Concrete constitutive model, calibration and applications. In *2013 SIMULIA Community Conference* (*SCC*), Vienna, Austria.

Wang, M. (2017). *Study on mechanical properties and ultimate load bearing capacity of exposed column base connections for rectangular hollow steel section* [Master's thesis]. Tianjin University, Tianjin.

Wang, Z., Wang, L., Li, L., & Wang, J. (2014). Failure mechanism of tunnel lining joints and bolts with uneven longitudinal ground settlement. *Tunnelling and Underground Space Technology*, *40*, 300–308. https://doi.org/10.1016/j.tust.2013.10.007

Weng, X., Sun, Y., Zhang, Y., Niu, H., Liu, X., & Dong, Y. (2019). Physical modeling of wetting-induced collapse of shield tunnelling in loess strata. *Tunnelling and Underground Space Technology*, *90*, 208–219. https://doi.org/10.1016/j.tust.2019.05.004

Xu, G., Zhang, J., Wang, S., Zhang, C., & Yao, C. (2024). The progressive failure features of shield tunnel lining with large section. *Engineering Failure Analysis*, *164*, Article 108687. https://doi.org/10.1016/j.engfailanal.2024.108687

Yan, Q., Deng, Z., Zhang, Y., & Yang, W. (2017). Failure characteristics of joint bolts in shield tunnels subjected to impact loads from a derailed train. *Shock and Vibration*, *2017*(1), Article 2829783. https://doi.org/10.1155/2017/2829783

Yan, Q., Xu, Y., Zhang, W., Geng, P., & Yang, W. (2018). Numerical analysis of the cracking and failure behaviors of segmental lining structure of an underwater shield tunnel subjected to a derailed high-speed train impact. *Tunnelling and Underground Space Technology*, *72*, 41–54. https://doi.org/10.1016/j.tust.2017.11.002

Ye, Z., & Liu, H. (2021). Investigating the relationship between erosion-induced structural damage and lining displacement parameters in shield tunnelling. *Computers and Geotechnics*, *133*, Article 104041. https://doi.org/10.1016/j.compgeo.2021.104041

Zhang, J., Wang, Q., Hu, S., & Wang, C. (2008). Parameters verification of concrete damaged plastic model of ABAQUS. *Building Structure*, *38*(8), 127–130.

Zhang, D. M., Xie, X. C., Zhou, M. L., Huang, Z. K., & Zhang, D. M. (2021). An incident of water and soil gushing in a metro tunnel due to high water pressure in sandy silt. *Engineering Failure Analysis*, *121*, Article 105196. https://doi.org/10.1016/j.engfailanal.2020.105196

Zhao, T., Liu, W., & Ye, Z. (2017). Effects of water inrush from tunnel excavation face on the deformation and mechanical performance of shield tunnel segment joints. *Advances in Civil Engineering*, *2017*, Article 5913640. https://doi.org/10.1155/2017/5913640

Zheng, G., Cui, T., & Ting, X. (2015). Mechanism of progressive collapse induced by partial failure of shield tunnels in sandy soil. *Chinese Journal of Geotechnical Engineering*, *37*(9), 1556–1571.

Zheng, G., Cui, T., Cheng, X., Diao, Y., Zhang, T., Sun, J., & Ge, L. (2017). Study of the collapse mechanism of shield tunnels due to the failure of segments in sandy ground. *Engineering Failure Analysis*, *79*, 464–490. https://doi.org/10.1016/j.engfailanal.2017.04.030

Zheng, G., Chen, Z., Zhang, T., Wang, K., & Diao, Y. (2024a). Experimental study on the erosion morphology of fine sand under converging flow considering the impact of soil effective stress. *Acta Geotechnica*, *19*(2), 1129–1135. https://doi.org/10.1007/s11440-023-01985-3

Zheng, G., Chen, Z., Zhang, T., Qiu, H., Wang, K., & Diao, Y. (2024b). Particle-scale study on backward erosion of multilayer erodible medium under converging flow: experimental tests and numerical modelling. *Acta Geotechnica*, *19*(10), 7075–7087. https://doi.org/10.1007/s11440-024-02370-4

Zhou, H. (2011). *Theoretical study and test on mechanic behavior of lining segment in shield tunnel* [Doctoral thesis]. Dalian University of Technology, Dalian.

Zhu, R. (2021). *Mechanism behind failure propagation of two closely spaced shield tunnels and division of influence area* [Master's thesis]. Tianjin University, Tianjin.